

RESEARCH ARTICLE | JANUARY 27 2023

Influence of nucleation on cavitation inception in tip leakage flows

Special Collection: [Cavitation](#)

P. S. Russell   ; L. Barbaca  ; J. A. Venning  ; B. W. Pearce  ; P. A. Brandner 

 Check for updates

Physics of Fluids 35, 013341 (2023)

<https://doi.org/10.1063/5.0132034>



View
Online



Export
Citation

CrossMark

Influence of nucleation on cavitation inception in tip leakage flows

Cite as: Phys. Fluids **35**, 013341 (2023); doi: [10.1063/5.0132034](https://doi.org/10.1063/5.0132034)

Submitted: 26 October 2022 · Accepted: 19 December 2022 ·

Published Online: 27 January 2023



View Online



Export Citation



CrossMark

P. S. Russell,^{a)} L. Barbaca, J. A. Venning, B. W. Pearce, and P. A. Brandner

AFFILIATIONS

Australian Maritime College, University of Tasmania, Tasmania, Australia

Note: This paper is part of the special topic, Cavitation.

^{a)} Author to whom correspondence should be addressed: Patrick.Russell@utas.edu.au

ABSTRACT

Cavitation in a tip leakage flow is experimentally investigated in a cavitation tunnel using a stationary hydrofoil analogy. The experiments were performed for different tip clearances ($\tau = \text{gap height}/\text{maximum profile thickness}$) and hydrofoil incidences (α). The chord-based Reynolds number remained fixed at $Re = 3 \times 10^6$. The influence of nucleation on both inception and developed cavitation is evaluated by performing tests with two populations of freestream nuclei: a low concentration with strong critical tensions for activation and a high concentration with weak critical tensions. These populations represent the extremes that would be expected in practical tip leakage flows. Cavitation was characterized using high-speed imaging and acoustic measurements. Following a survey of developed cavitation topology for a range τ and α values, $\alpha = 6^\circ$ was selected for further investigation of cavitation inception as it demonstrated a rich variety of physical processes. From the acoustic measurements, the worst performance in terms of cavitation inception was observed at an intermediate gap height of around $\tau = 0.6\text{--}0.8$ for the “strong water” case. Broadly, cavitation and inception is intermittent when nuclei are sparse, becoming continuous as additional nuclei are introduced. While a continuous cavity in the seeded flow resulted in a higher baseline acoustic signature, sparse populations allow the leakage vortex to sustain tension, which can result in extremely loud incipient events. Optimization of gap height will, therefore, depend on the expected nuclei population during operation.

Published under an exclusive license by AIP Publishing. <https://doi.org/10.1063/5.0132034>

INTRODUCTION

Flow in the gap between the tip of a rotating blade and static casing is a feature observed in many fluid mechanics applications, most prominently in axial turbomachinery and ducted propulsors.^{1,2} Due to the complexity of the flow through the gap and a high blade-tip velocity, the tip leakage flow (TLF) is often a feature with the global pressure minimum, and consequently, highest susceptibility to the inception of cavitation.

Cavitation in tip leakage flows can occur in many forms, but for a well-designed gap geometry, cavitation inception is most likely in the tip leakage vortex (TLV). However, experimental studies using a rotating model, particularly at large Reynolds number, report cavitation inception in the small vortical filaments originating from the tip trailing edge³ and the jetting shear layer on the suction side of the hydrofoil.⁴

While the mean pressure in the cores of the vortical filaments is higher than that in the core of a nominally stronger TLV, interactions between the weaker filaments and the TLV can lead to the filament stretching, and a sudden instantaneous drop in the filament core

pressure can occur. Consequently, instantaneous pressure in the core of the filaments may decrease below that in the core of the TLV, making the vortical filaments sites of the global pressure minimum and cavitation inception.^{3,5} This transient type of small-scale cavitation inception has been documented in axisymmetric jets^{6,7} as well as in plane shear layers⁸ or behind a backward-facing step.^{9–11}

The TLF is characterized by a multitude of interacting flow features, which affect the inception of cavitation. Unbounded finite-span lifting surfaces generate trailing vortices due to spanwise flows near the tip, driven by the pressure difference between the two sides of the hydrofoil. This reduces the lift generated in the vicinity of the tip, increases the drag of the wing, and provides a mechanism for the downstream transport of vorticity from the hydrofoil surface.¹² The cores of these trailing vortices are characterized by high rotation rates and low pressures. As confinement is introduced in the vicinity of the tip, and flow through the gap reduces, the pressure difference between the sides of the hydrofoil increases.¹³ For small clearances, the leakage flow is suppressed, producing a more two-dimensional (2D) flow, higher lift, and a weaker trailing vortex. However, the difference in

pressure increases the angle between the flow through the gap and the free-stream flow, which may induce local separation at the trailing edge.¹⁴ It may also induce development of low-pressure areas at the leading edge and flow separation within the gap, which promote cavitation.¹⁵ Rounding of the edge on the pressure side of the hydrofoil tip can be utilized to mitigate flow separation and cavitation within the gap; however, it is often accompanied by increased shear on the foil suction side contributing vorticity to the TLV.¹⁶

Treatments to the pump or duct casing, such as circumferential grooves, have been applied in an effort to mitigate cavitation, but must be implemented with care as these regions can act as sites for re-nucleation of cavitation once inception, and tend to be ineffective at larger gap clearances.¹⁷ Likewise, modification of the tip geometry such as tip extensions and other tip treatments can offer benefits, but their effectiveness varies greatly with the gap clearance.¹

In order to reduce modeling complexity, single stationary hydrofoil analogies of multi-bladed rotating geometries have been explored both experimentally^{15,18–21} and numerically.^{14,22–24} Although, many aspects of the flow are not captured with a single hydrofoil analogy, these approximations have proved to be a useful tool in exploring a number of flow features that are also observed experimentally in the rotating flows they emulate (Fig. 1).²⁵

To date, the effect of the nuclei content on cavitation in these flows has not been appropriately addressed. In order for the cavitation inception to occur, the water must contain sites of weakness, also termed “nuclei,” which are typically found in the form of microbubbles. It has been shown that nuclei content has a significant effect on cavitation inception and the dynamics of developed cavitation in model testing^{13,26–28} and, therefore, a capability to precisely control and/or measure the water nuclei content is mandatory in hydrodynamic facilities for studying cavitation.

Gopalan *et al.*¹⁹ studied the effect of seeding the TLF with nuclei generated via electrolysis and observed a 50-fold increase in the cavitation event rate between the seeded and unseeded flow for the same cavitation number. However, the size of the nuclei were large, particularly when compared to the structures within the flow and the overall size of the model. Russell *et al.*^{15,29} reported studies of the TLF cavitation for a hydrofoil model with a square-edged tip for a flow with the natural nuclei (deplete) content and a flow artificially seeded with an abundant polydisperse nuclei population. They note that the topology

and acoustic signature of developed cavitation remain similar for the two nuclei populations. However, differences in desinent behavior were observed, where for the nuclei deplete flow, desinence is sudden and for nuclei abundant flow, it is more gradual.

The effect of nuclei on cavitation inception has been investigated in more detail for a three-dimensional (3D) hydrofoil in an unbounded flow. In this case, the most likely site of cavitation inception is within the low-pressure core of the vortex trailing from the hydrofoil tip. This phenomenon is referred to as tip vortex cavitation (TVC). Earlier experimental studies on the effect of nuclei on the TVC inception were performed by indirectly controlling the nuclei content via the water dissolved gas content^{5,30} or via microbubble injection into the test flow.^{31,32} Recently, Khoo *et al.*²⁸ reported a study of TVC inception for the natural and two types of seeded nuclei populations (polydisperse and monodisperse). They describe the effect of nuclei concentration and size distribution on the location of inception within the vortex core and the flow acoustic signature. Nuclei size was observed not only to influence inception due to the size-dependent critical pressure but also the process of nuclei capture by the vortex. Similar measurements and nuclei populations will be explored here in the context of a leakage flow.

Prior studies at the Australian Maritime College Cavitation (AMC) Research Laboratory of tip leakage flows were performed using a NACA 0012 hydrofoil model equipped with interchangeable square-edge tips. These tests experienced premature cavitation in the gap, local sources of nucleation at the discontinuity between the tip and the hydrofoil main body, and sheet cavitation at the hydrofoil base due to the use of a thicker NACA 0040 foil section to prevent model vibration.^{15,29} To alleviate these issues, a new hydrofoil model with a custom-designed section and a complex tip rounding has been designed for the present work. Additionally, to remove nucleation from discontinuities, a new experimental apparatus has been developed to traverse the hydrofoil within the test section, enabling continuous adjustment of the hydrofoil incidence and the tip clearance.

Common to many previous studies of the TLF is the use of hydrofoil models with symmetric sections.^{15,21,29} The topology of the TLF observed in these studies was characterized by a well-defined TLV, but lacking secondary vortical structures typically observed in the experiments with a rotating model.^{3,4} The lack of secondary structures can be attributed to the low lift generated by symmetric sections



FIG. 1. Cavitation in a tip leakage flow for a truncated “square” edge tip and a tip with a rounded profile: (a) NACA0012 profile for a maximum thickness to gap ratio of $\tau = 0.16$, $\sigma = 1$, and $\alpha = 5^\circ$ and (b) custom profile, analogous to a NACA66-012(mod) thickness profile with a NACA $a = 0.8$ camber line, $\sigma = 1$, and $\tau = 0.2$.

and consequent less intense flow through the gap. A solution to this issue is to increase the section incidence α . However, due to the low ratio of the sectional lift coefficient to the minimum pressure coefficient on the foil suction side, an increase in α resulted in the onset of cavitation on the hydrofoil face, which was detrimental to characterization of the inception in the TLF. An alternative method to increase the section lift is to apply camber.

For a stationary hydrofoil analogy to emulate the flow features of a high Reynolds number rotating TLF, distribution of sectional profiles along the hydrofoil model span has to be carefully considered. A particular difference, with regard to cavitation inception, stems from an increase in circumferential velocity from the root toward the tip of a rotating blade. Due to the circumferential velocity distribution, the tip region of a rotating blade is the most likely site of cavitation inception. In contrast, a stationary hydrofoil model experiences a uniform inflow, which can lead to cavitation forming at the hydrofoil root. This problem is compounded by the requirements for low model vibration and tip deflection, which in prior experiments at the AMC was addressed via increasing the thickness of the hydrofoil model toward the root.^{15,29} The added thickness resulted in a decrease in the minimum pressure about the root section, and for some conditions, the root was found to be the site of global cavitation inception. This had a detrimental effect on the acoustic characterization of the TLF cavitation, as the noise generated by collapse and condensation of the cavity forming at the root obscured the acoustic signature of cavitation inception in the TLF.¹⁵ A potential solution for this issue is to twist the model, i.e., reduce the incidence of the root section, resulting in a complex three-dimensional geometry. Instead, for the current work, it was elected to maintain the pressure distribution on the suction side by balancing the increase in the section thickness with a decrease in the section camber.

Based on these considerations, a hydrofoil model geometry with section profiles designed using custom tools and evaluated using XFOil³³ has been developed. The model is designed with a constant section profile for the outer third of the span. The section profile varies across the remainder of the span, with the section thickness increasing linearly toward the root to ensure adequate stiffness of the model. The hydrofoil section is optimized for the maximum ratio of the lift to the negative local pressure maximum.

Tip leakage cavitation inception for the optimized hydrofoil will be explored using rigorous modeling of different free-stream nuclei populations. For the current work, these include the natural nuclei population and an abundant polydisperse population of comparatively large nuclei. These populations represent the two extremes in which turbomachinery and ducted propulsors typically operate and highlights the differences in the cavitation inception dynamics induced by variation of the water nuclei content.

EXPERIMENTAL SETUP

The experiments were performed in the variable pressure water tunnel at the University of Tasmania. The tunnel test section is $0.6 \times 0.6 \text{ m}^2$ at the entrance and 2.6 m long. The test section ceiling is horizontal with the floor sloping 20 mm over the length to maintain nominally constant speed and a zero-stream-wise pressure gradient. The operating velocity and pressure are controlled independently, with ranges from 2 to 13 m/s and 4 to 400 kPa absolute, respectively. The test section velocity is measured from the calibrated contraction differential pressure and has been measured to be spatially uniform to

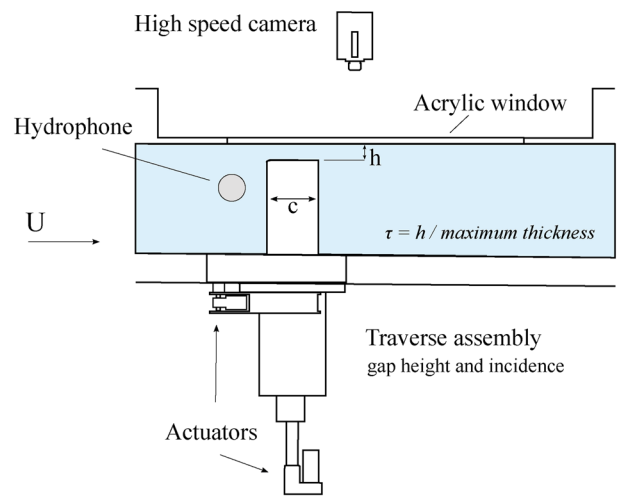


FIG. 2. Schematic of the experiment.

within 0.5%, with a temporal variation of less than 0.2%, and a free stream turbulence intensity of 0.5%. The tunnel volume is 365 m³ and is filled with demineralized water. The water dissolved oxygen content is measured using a membrane sensor and kept at approximately 30% of atmospheric saturation to ensure the nuclei population remains stable. Optical access is provided through acrylic windows on each side of the test section. Further details on the facility are provided by Brandner *et al.*^{34,35} The hydrofoil leading edge was located 900 mm downstream of the test section entrance. At this position, the unperturbed wall boundary layer thickness has been measured to be 19 mm.³⁶

Tip gap flow was developed between the ceiling of the tunnel test section and the end of a stationary hydrofoil, as schematically represented in Fig. 2.

The hydrofoil model has a chord length of $c = 280 \text{ mm}$. Section profiles for the model were designed using customized definitions for thickness and camber³⁷ and evaluated using the 2D numerical code XFOil.³³ The tip section is analogous to a NACA 66-012 mod section with a NACA $a = 0.8$ rooftop camber profile, resulting in an overall flat pressure distribution with a maximum thickness of $t = 33.6 \text{ mm}$. Here, the pressure coefficient is defined as

$$C_p = \frac{p - p_\infty}{0.5\rho U_\infty^2},$$

and the sectional lift coefficient

$$C_l = l/0.5\rho U_\infty^2 c.$$

Section geometries at selected locations along the hydrofoil span are presented in Fig. 3 (3D model available in the supplementary material). A cambered profile was used to increase lift, and care was taken during the overall geometry designed to avoid cavitation on the face of the model. The section profile near the tip is held constant for a third of the hydrofoil span, but is thickened toward the base to reduce model vibration and any potential tip deflection under load. Ideally, the lift would remain constant along the span, but to maintain a similar

03 August 2023 06:22:46

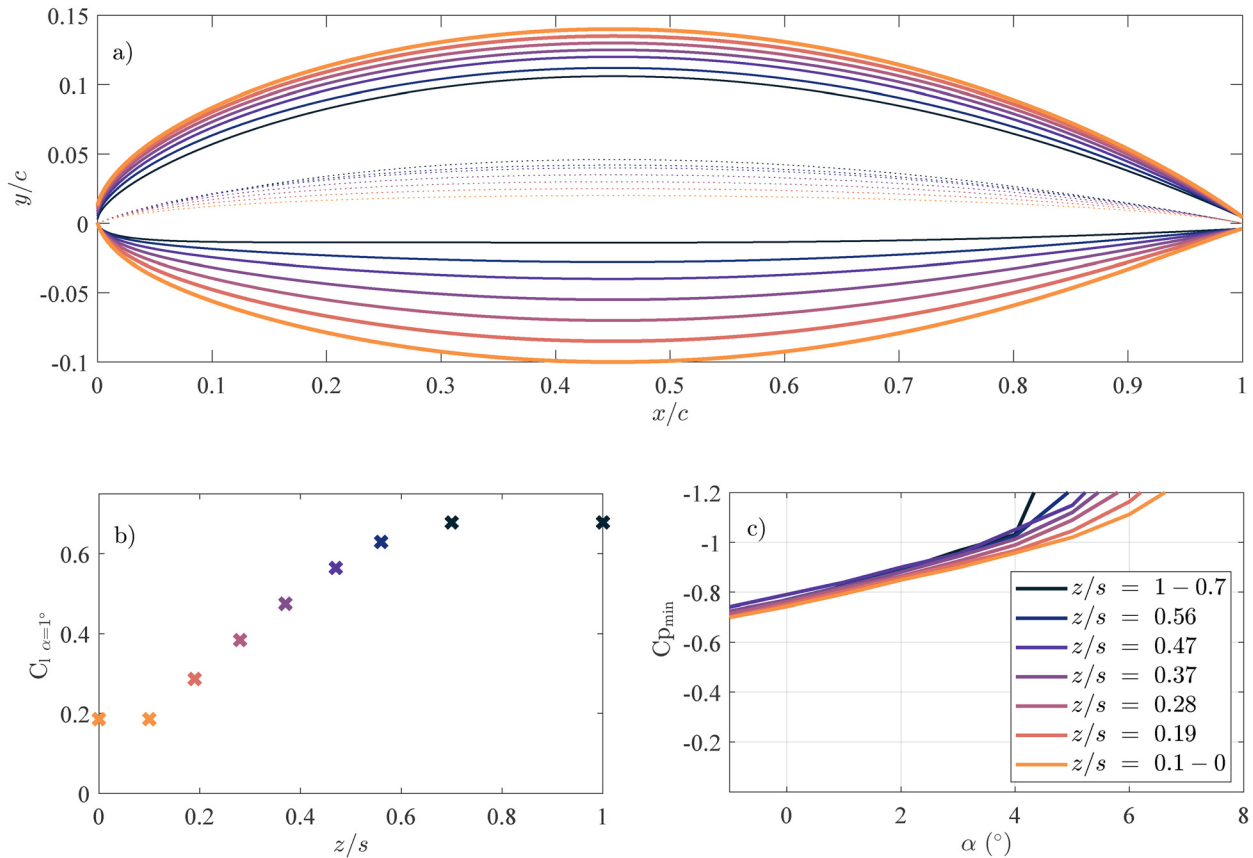


FIG. 3. (a) Section profiles and the camber curve of the hydrofoil model are presented at various locations along the model span. The tip section profile near the tip is held constant for approximately one third of the model span. (b) Section lift along the model span for $\alpha = 1^\circ$. (c) Minimum pressure coefficient against incidence for each section. By reducing camber and lift with increased thickness, the minimum C_p is kept relatively constant across the span.

minimum pressure as thickness increases, the lift also decreased toward the root. Coefficients from XFOIL of sectional lift C_l and minimum pressure $C_{p,min}$ for each section are presented in Fig. 3.

The hydrofoil and its mounting block were machined out of a single forged stainless steel billet. The mounting block is housed within an actuated assembly outside the tunnel and allows for a continuous adjustment of the tip gap (h) and the incidence (α) of the hydrofoil. The gap and the incidence adjustments were controlled using Tolomatic 32RSA-HT1 stepper motor electric linear actuators, driven by a Tolomatic ACS stepper driver motor controller, with a maximum thrust of 18.5 kN. The actuators have an accuracy of 0.01 mm across a 300 mm travel, and for the present work, the gap could be adjusted in the range $1 \leq h \leq 70$ mm to give an approximate normalized tip clearance range of $0.03 \leq \tau = h/t \leq 2$. The range of incidence achieved was $-10^\circ \leq \alpha \leq 10^\circ$.

High-speed imaging of the cavitation topology in the gap was acquired using a Phantom v2640 camera with a maximum resolution of 2048×1952 pixels, mounted above the tunnel test section (Fig. 4). The camera was equipped with a Nikon AF Nikkor 24 mm $f/2.8$ D lens with the images acquired at a cropped resolution of 2048×640 pixels at a sampling rate of 10 000 frames per second. Continuous

illumination was provided from two Efflux EFFI-BL-LITE-1M12P 650×650 mm² LED panels mounted to the side of the test section and three Veritas Constellation 120 LED lamps mounted above and to the side of the test section. The image acquisition was controlled via Phantom PCC 3.4.4 software. Optical access to the gap was provided through a 1150 mm long \times 215 mm wide acrylic window in the test section ceiling.

Acoustic measurements were obtained using a Brüel & Kjær Type 8103 hydrophone (voltage sensitivity $25.1 \mu\text{V}/\text{Pa}$) mounted in a flooded cavity (kept at the same pressure as the tunnel test section) beneath a 10 mm polyurethane diaphragm, with a 149 mm sensing diameter.³⁸ The hydrophone was mounted in the sidewall, 150 mm below the ceiling and approximately a chord length upstream of the hydrofoil leading edge. The signal was conditioned using a Brüel & Kjær Nexus conditioner and amplifier, which was also used to apply a 0.1 Hz–100 kHz bandpass filter. The filtered signal was acquired using a National Instruments PXIe-4497 card at a sampling rate of 204.8 kS/s. Each acoustic measurement was performed for a period of 60 s. The high-speed imaging and the acoustic measurements were triggered independently; however, the data were synchronized by recording the camera trigger signal along with the acoustics and using

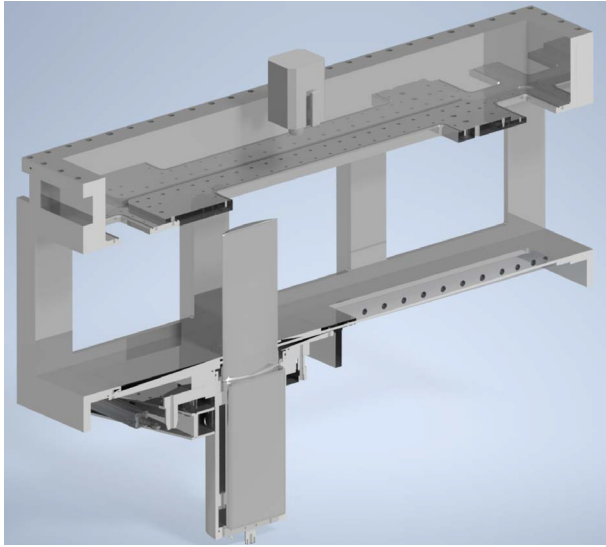


FIG. 4. 3D schematic of the experiment.

it to align the two datasets. The camera was operated with a post trigger, so that once an incipient event was manually observed or heard, the camera trigger could be activated (Fig. 4).

Experiments were performed for a hydrofoil chord-based Reynolds number, $Re = Uc/\nu = 3 \times 10^6$, where U is the mean flow velocity and ν is the water kinematic viscosity. The cavitation number is defined as $\sigma = (p - p_v)/0.5\rho U^2$, where p is the static pressure at the tunnel ceiling, p_v is the water vapor pressure, and ρ is the water density. The hydrofoil tip gap was non-dimensionalized by the maximum thickness of the hydrofoil tip section, $\tau = h/t$.

Two nuclei populations were used during the investigation: a sparse population of nuclei with very strong critical tensions for activation and an abundant population of weak nuclei. We term the first population as the “natural” or tunnel background nuclei population. These nuclei are ever present even when the water is strongly degassed. Small in size, these nuclei are below our ability to optically measure and were characterized via mechanical activation in a Cavitation Susceptibility Meter (CSM).³⁹ For a dissolved O_2 gas content of below 40% saturation atmospheric pressure, Khoo *et al.*³⁹ demonstrated that this population is practically invariant to tunnel operating conditions. The second population is comprised of polydisperse microbubble nuclei that are artificially seeded into the tunnel upstream of the contraction. Much larger in size, these nuclei have weak critical tensions. Microbubbles for artificial nuclei seeding are generated via rapid depressurization of supersaturated water through an orifice, with a device referred to as “mini-tube.”⁴⁰ An array of 10 mini-tube devices was utilized to generate a nuclei plume seeding the top third of the test section and 50 mm each side of the tunnel centerline. Each device produces microbubbles at a rate of $\approx 10^6$ Hz. This can produce a high concentration of active nuclei in the flow, so that we have termed this the abundant population of nuclei. The distribution of size and concentration in the test section was characterized by Russell *et al.*⁴¹ using Mie-Scattering Imaging (MSI). Nuclei size distributions for both the natural and abundant populations are presented in Fig. 5.

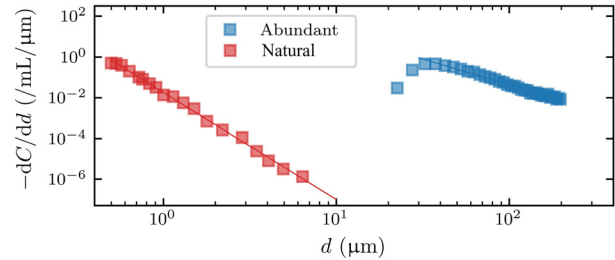


FIG. 5. Nuclei size distribution of the natural and abundant polydisperse populations used in the experiments. These distributions may be integrated from a lower bound corresponding to a given tension to find the concentration of nuclei whose critical tensions are weaker than the limit.

RESULTS AND DISCUSSION

Developed cavitation topology

To perform an initial survey of the TLV topology across a range of α and τ values for both nuclei populations, high-speed imaging of developed cavitation ($\sigma = 1.35$) was utilized. Extracted frames from the high-speed recordings obtained at various conditions are presented in Figs. 6 and 7 (Multimedia view).

For the natural nuclei population, with the hydrofoil at zero incidence, thin intermittent incipient structures are observed in the TLV downstream of the foil. These structures rapidly grow from the initial size of the nucleus to form a short cavity that is simultaneously transported downstream. The location of inception has a stochastic character. From visual observation of high-speed data, this appears to shift downstream with an increase in τ .

With the introduction of nuclei, cavitation in the TLV becomes less intermittent and the inception location moves closer to the hydrofoil. This can be attributed to a high availability of larger nuclei. These bubbles have a critical pressure close to p_v , incepting almost instantly as they reach the low-pressure core of the TLV and continuously merging into the main cavity volume. Similar to the natural nuclei case, the cavity leading edge shifts downstream along the hydrofoil chord with an increase in τ . This phenomenon is more easily observed in the seeded flow due to the less intermittent nature of cavitation.

For $\alpha = 3^\circ$, similar trends were observed. The TLV is further deflected from the hydrofoil due to increased flow through the gap. Generally, the cavities are thicker than those observed for $\alpha = 0^\circ$, reflecting the increase in the diameter of the core of the TLV with increase in α and related increase in lift. For the flow with natural nuclei populations, incipient events are less intermittent than at $\alpha = 0^\circ$, with subsequent events occasionally incepting before the prior events are washed away. In such instances, the new cavity upstream grows rapidly down along the TLV and merges with the prior cavity. This merging is characterized by a spike in the acoustic signature and will be further discussed in Incipient cavitation events in a nuclei deplete flow.

For the low α values, the TLV is strong compared to the other sources of vorticity so that it remains well defined and with little oscillations in its trajectory, as shown in Fig. 6. With an increase in incidence to $\alpha = 6^\circ$, the topology of the TLV becomes more complex with the flow through the gap beginning to noticeably alter the trajectory of the TLV (see Fig. 7). For large τ values, the cavity is

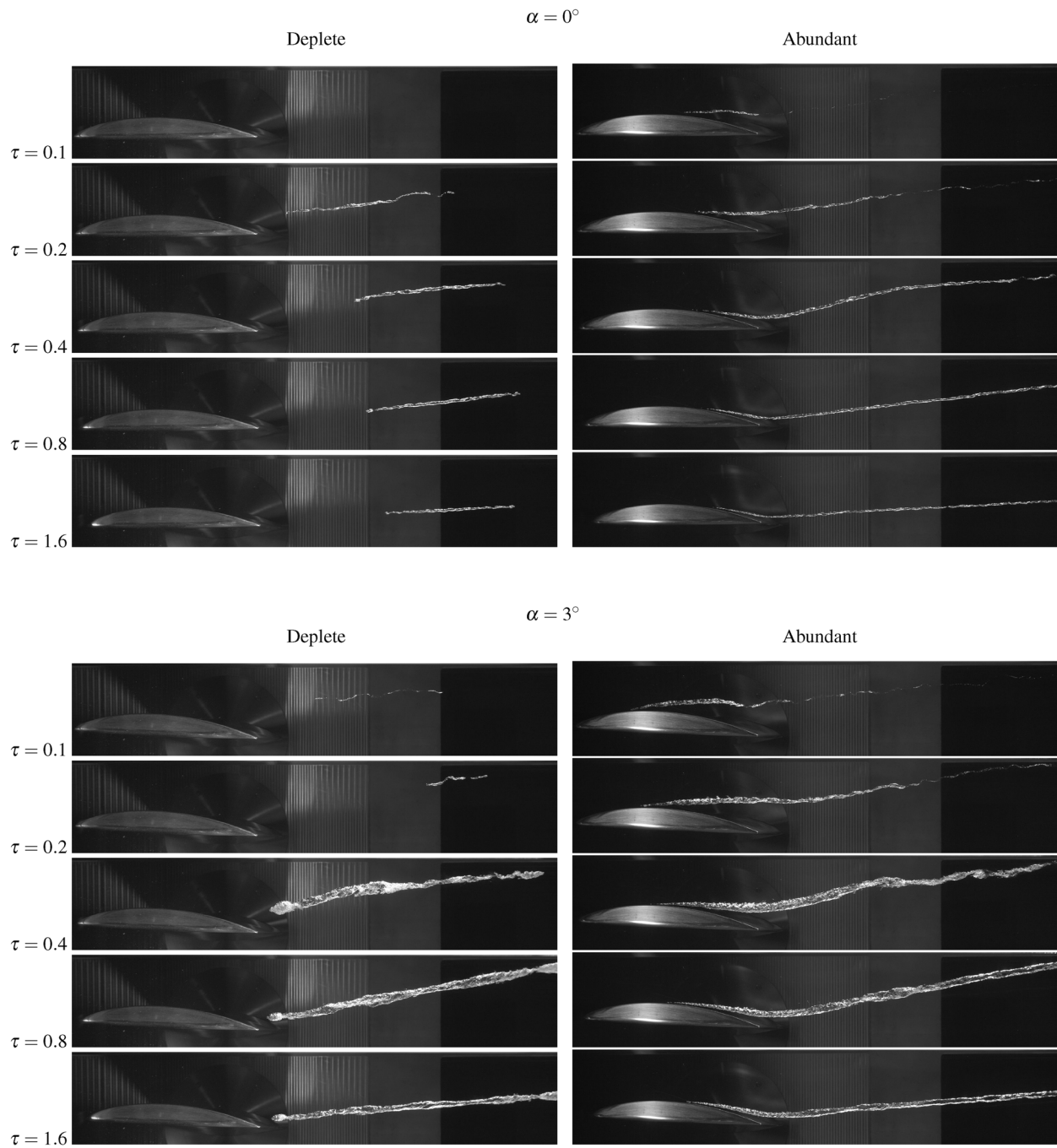


FIG. 6. Developed cavitation topology at $\alpha = 0^\circ$ and 3° , $Re = 3 \times 10^6$, and $\sigma = 1.35$ for both the natural and abundant population of free-stream nuclei.

deformed into a twisted helical ribbon resulting from the merger of the TLV and the vortex originating from the tip trailing edge (Fig. 7). The helical merger of these vortices indicates their co-rotating orientation.

For the seeded flow at $\alpha = 6^\circ$, traveling bubble and sheet cavitation were observed within the gap. Cavitation within the gap nucleates

braids of shed vorticity, associated with a jetting shear layer on the suction side of the tip, which bridges the gap and TLV cavities. These braids indicate the presence of sources of secondary vorticity, often postulated as the sites of cavitation inception in the TLF due to the large instantaneous variations in the pressure.^{3,4} However, the inception for seeded flow at high values of σ was not resolved with sufficient

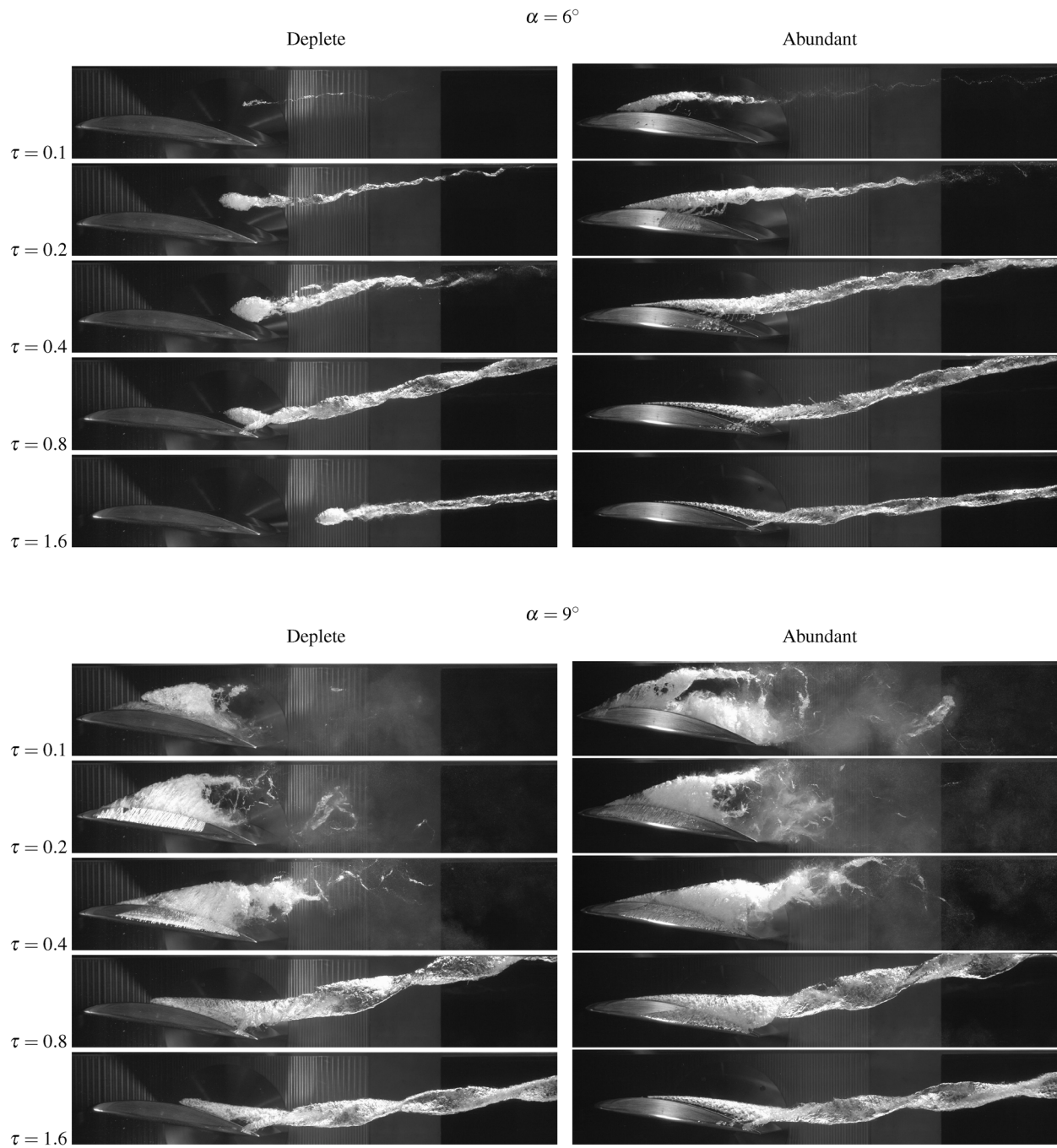


FIG. 7. Developed cavitation topology at $\alpha = 6^\circ$ and 9° , $Re = 3 \times 10^6$, and $\sigma = 1.35$ for both the natural and abundant population of free-stream nuclei. High-speed data of select conditions for $\alpha = 6^\circ$ is presented in a video format, comparing cavitation topology with and without nuclei seeding. Playback rate is 30 frames per second, with a sampling rate of 10 000 fps. Multimedia view: <https://doi.org/10.1063/5.0132034.1>

detail to ascertain whether these are indeed the sites of cavitation inception. This will be the subject of future work.

Although cavitation was well developed, it was pleasing to observe only limited cavitation within the gap for the natural nuclei

population flow. This is a marked improvement over the geometry previously tested with a square tip, which was dominated by the cavity formed from separated flow over the tip^{15,29} (see Fig. 1). For large τ , where gap cavitation was present, it was mainly associated with the

small radius near the trailing edge due to the limitations imposed by a decrease in the section thickness. As τ is reduced, more lift is retained, and the cavity moves forward above the tip. At $\alpha = 6^\circ$, cavitation in the gap for small τ is suppressed due to reduced flow through the gap.

Further increase in the incidence to $\alpha = 9^\circ$ resulted in increased intensity of the tip trailing edge vortex for large τ values. For $\tau \leq 0.4$, a greater proportion of the lift is maintained at the tip so that cavitation on the hydrofoil face was observed. The incidence of the flow through the gap, coupled with the instabilities from the collapse of cloud cavities now forming on the hydrofoil face, induced TLV bursting and complete disintegration with a decrease in τ .

Considering the high-speed images across the range of incidence tested, perturbations to the tip leakage vortex cavity generally reduce as the tip gap widens. The TLV follows a more consistent trajectory,

with the cavity assuming a more transparent appearance as the effects of confinement and influence of the wall boundary layer turbulence diminishes. To track the trajectory of the TLV in more detail, high-speed footage for the abundantly seeded population at $\sigma = 6$ was analyzed. The buoyant forces experienced by the microbubble nuclei in the seeded population are small; however, the pressure gradients around the tip leakage vortex are sufficient to draw bubbles into the vortex core where they coalesce. Their concentration in the flow is high enough that large bubbles of gas develop and the trajectory of the leakage vortex can be visualized. The trajectory of the leakage vortex was measured for several values of τ at $\alpha = 0^\circ, 3^\circ$, and 6° . A summary of the mean vortex trajectory superimposed on a single frame of the high-speed footage is presented in Fig. 8. The contrast of the images during the analysis was enhanced by taking the maximum intensity on a pixel by pixel basis over 1000 images. This also ensured that the

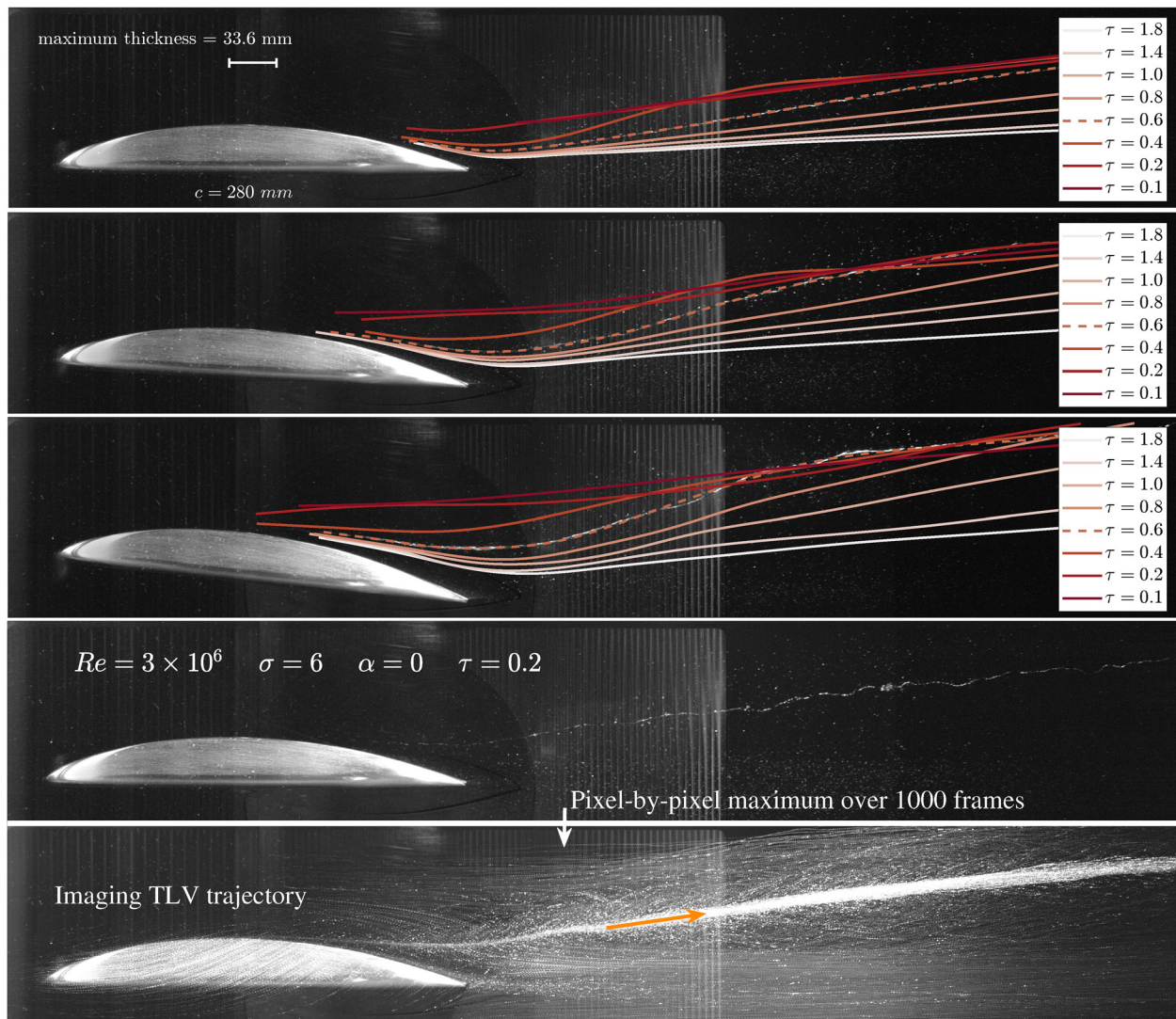


FIG. 8. Trajectory of the leakage vortex for $\alpha = 0^\circ$ (top), $\alpha = 3^\circ$, and $\alpha = 6^\circ$ for varying τ with abundant cavitation nuclei for $\sigma = 6$.

03 August 2023 06:22:46

trajectory was not influenced by perturbations captured in a single image, and the mean trajectory was extracted.

The primary feature to be observed from Fig. 8 is the deviation/kink in the TLV trajectory. Its location varied with gap height so that as it reduced the distance between the tip leakage vortex trajectory and the trailing edge tip increased. These trends persist across the range of α tested. A component of this deviation is discussed in detail by Boulon *et al.*¹⁸ whereby the image vortex leads to locally increased incidence at the tip. The effect strengthens as gap height is reduced. However, these earlier experiments relate to an elliptic planform model whose diminishing chord near the tip is less able to maintain a pressure difference. With the present geometry, this pressure differential will further alter the flow and lead to jetting through the gap. From the processed images used to measure the trajectory, streak-lines can be observed from illuminated microbubble nuclei as they pass over the model. In a small area near the trailing edge extending into the wake, a region of low momentum flow is visible as flow over the tip separated from the low-pressure face. These regions grew larger for smaller gap heights, particularly at high incidence.

While the magnitude of the deviation changed with incidence, it is observed that the downstream location of this kink does not change with incidence, and therefore, lift. This transition also begins to occur for a gap height close to $\tau = 0.6$ —the dashed line in Fig. 8—close to the equivalent normalized boundary layer thickness of $\tau = 0.57$. Together, these suggest that this process occurs as the leakage vortex begins to interact with the boundary layer. As τ is reduced, the leakage vortex eventually becomes immersed inside the boundary layer, and the high momentum fluid brought over the tip from the pressure side leads to separation of the leakage vortex from the model further upstream. This initially moves the trajectory of leakage vortex away from the model before it corrects toward a course similar to the leakage vortex at larger gap heights. An extreme case can be seen in Fig. 7, for $\alpha = 6^\circ$, $\tau = 0.1$, and $\sigma = 1.35$, where the presence of the cavity allows the TLV to be transported well above the tip in the image by mid-chord.

From these observations of the developed cavitation topology, an incidence of $\alpha = 6^\circ$ was selected for further investigation of cavitation inception for a range of conditions.

Incipient cavitation events in a nuclei deplete flow

Inception in deplete flows involves intermittent activation of nuclei with subsequent growth of discrete vortical cavities with simultaneous downstream transport. A typical acoustic signature and topology of an incipient event at a high cavitation number ($\sigma = 6$, $\alpha = 6^\circ$) is presented in Fig. 9. A selection of four extracted frames from the high-speed imaging outlines the development of the cavity. The accompanying time series of the acoustic signal is plotted below, and the time corresponding to each image is annotated.

To resolve the frequencies emitted during inception, a wavelet transform of the unfiltered time series is analyzed and presented in Fig. 9(e). It should be noted that the tunnel is a confined environment, and that the frequencies present in the acoustic signature may be affected by reverberation. Prior to an isolated nuclei activation event, the time series contained very little acoustic energy. During the growth phase of the cavity, a peak in the wavelet is observed at $f = 1.5$ kHz. Without sudden collapse of the cavity or any significant cavity breakup, the noise emitted during the inception is relatively low, with the acoustic pressure of the order of 100 Pa. Following the initial

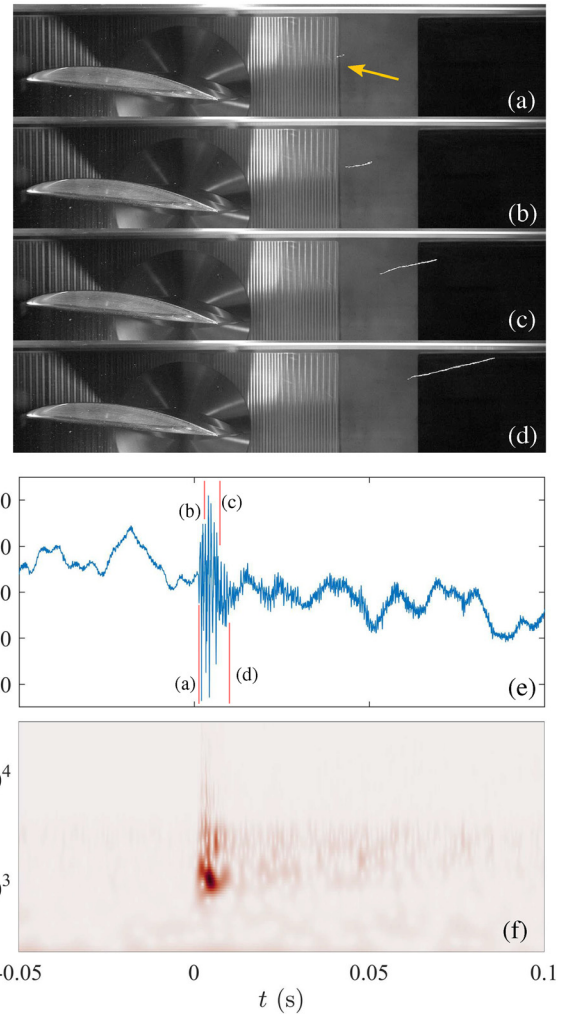


FIG. 9. Sequence of images for a typical inception event in a deplete flow, with companion acoustic time series and wavelet transform at $Re = 3 \times 10^6$, $\sigma = 6$, $\alpha = 6^\circ$, $\tau = 0.8$. (a)–(d) Still images from the high-speed data, (e) raw acoustic time series, and (f) wavelet spectrogram of the acoustic data.

growth, ongoing acoustic emissions remain presumably, due to surface modulations, evident in the high-speed imaging. This signature persists for a period of the order of 0.1–1 ms as the cavity is convected downstream by the flow. The oscillation and migration of the cavity downstream is associated with an increase in wavelet power in the range $1 \text{ kHz} \leq f \leq 5 \text{ kHz}$. Frequencies in this range agree with the results measured by Gopalan *et al.*¹⁹ for incipient cavities in similar experiments on tip gap flow. A second peak was also observed in this work at higher frequencies in the range of 17–20 kHz, which was attributed to fragmentation of the cavitation bubble. This was observed at smaller gap heights ($\tau < 0.6$) where unsteadiness from the boundary layer led to increased cavity modulation and fragmentation. However, at larger gap heights, less fragmentation occurred and little power was observed at these high frequencies, similar to the data presented in Fig. 9(e).

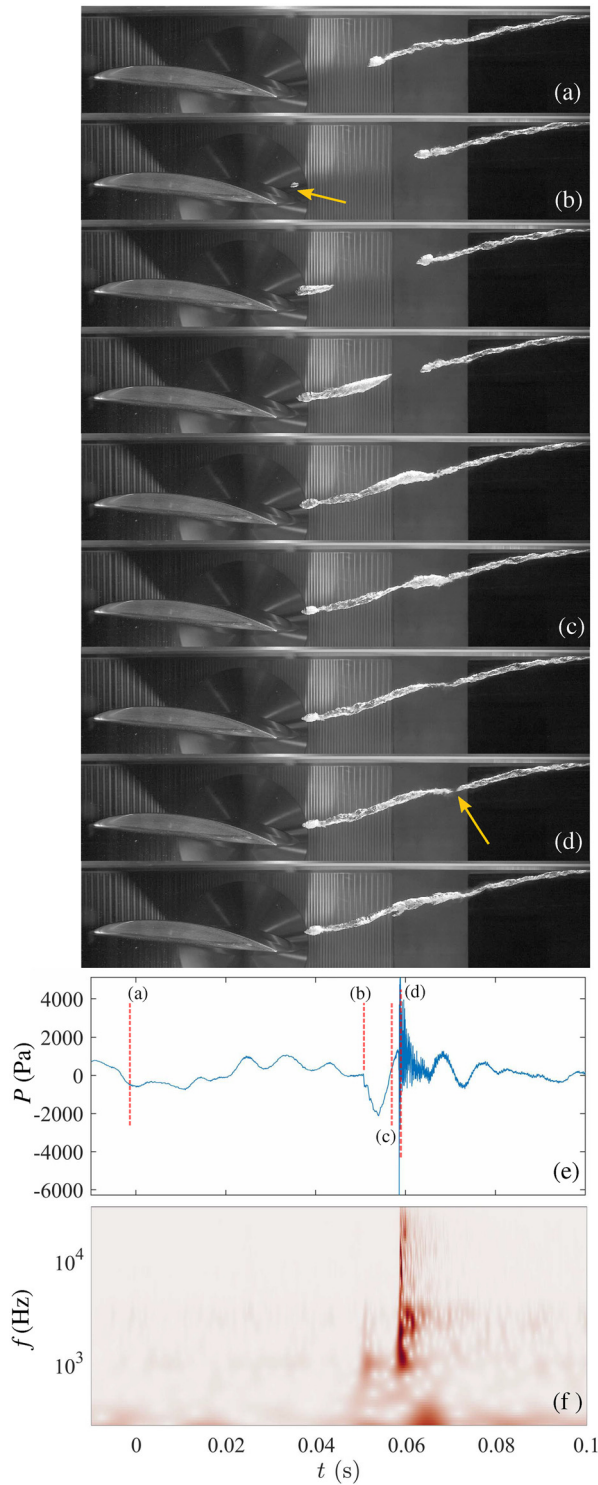


FIG. 10. Sequence of images for a typical inception event with companion acoustic time series and wavelet transform at $Re = 3 \times 10^5$, $\sigma = 2$, $\alpha = 6^\circ$, $\tau = 0.8$. (a)–(d) Still images from the high-speed data, (e) raw acoustic time series, and (f) wavelet spectrogram of the acoustic data.

An identical analysis was repeated for the same flow conditions, but at $\sigma = 2$ (see Fig. 10). At this cavitation number, the decrease in the mean core pressure of the TLV renders a larger proportion of the nuclei contained within the natural population susceptible to inception. Consequently, while the incipient events are still intermittent, there is an almost persistent overlap between the desinence of one event and the inception of a subsequent event. An incipient event grows rapidly along the TLV and merges with the previous cavity downstream. The acoustic signature during the growth phase resembles that at the higher σ in terms of both amplitude and frequency. However, as the growing cavity impinges on the leading edge of the previous one, it triggers a momentary collapse at the location of the connection. The shock wave emitted during the cavity collapse is characterized by a spike in the acoustic pressure with an order of magnitude higher amplitude than that of any other noise sources (~ 2000 Pa in Fig. 10 compared to ~ 100 Pa in Fig. 9). This is followed by a period of elevated acoustic signature associated with rebound and oscillation along the cavity. As the effect of merging decays, the acoustic signature returns to a level characteristic of the continuous TLV cavitation.

Overall sound pressure level (SPL) for flow with the natural nuclei population, calculated from a 60 s acoustic recording, is plotted in Fig. 11(a) for a range of σ and τ . Generally, the SPL increases as the

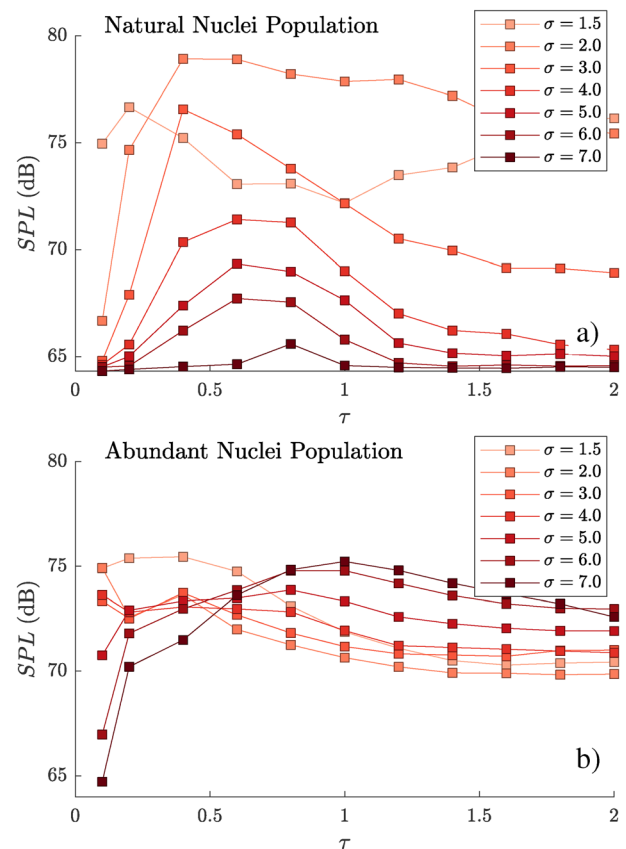


FIG. 11. (a) Overall sound pressure level for the unseeded flow across a range of σ and τ at $\alpha = 6^\circ$ and $Re = 3 \times 10^5$ are presented. (b) Similar measurements for flow with a seeded nuclei population are also plotted.

cavitation number is reduced, except for the lowest value tested ($\sigma = 1.5$). At this σ value, the TLV cavity was now ever-present. The close proximity of the cavity leading edge limits the growth of activated nuclei before merging with the main cavity. The small scale of new cavities results in the less severe collapse events during cavity merging, and hence, a lower acoustic signature. The SPL also generally increases with decreasing τ , reaching a maximum that is dependent on σ . The sound pressure level drops dramatically as the leakage flow within the gap is suppressed. For incipient cavitation at about $\sigma = 0.7$, the maximum SPL occurs for $\tau \approx 0.8$. This is in agreement with the observation of Dreyer *et al.*²¹ who demonstrated a specific gap width for which the vortex intensity reaches a maximum and is most prone to cavitation. They show that this unfavorable clearance ratio changes with incidence. Overall, these peaks occur between $0.4 \leq \tau \leq 1$. From Fig. 11(a) for $\tau = 0.8$, cavitation persists even for the highest cavitation number tested, $\sigma = 7$. Due to the mechanical limitations of the facility, a condition free of inception events could not be attained at this Reynolds number, incidence, and gap height combination. Persistent acoustic noise at lower cavitation numbers was observed across a range of τ .

High-pass filtered acoustic data were also analyzed to measure the acoustic event rate by detecting the peaks in the time series. To obtain the event rate, acoustic data were first bandpass filtered ($f_{pass} = 1 - 10$ kHz) and then interrogated to find the locations where the pressure increase between the subsequent points was above a threshold value of 50 Pa. This can happen multiple times during a single event, so, only events more than 10 ms apart were counted. Within reasonable limits, the inception event rate was insensitive to the choice of detection threshold. The raw acoustic time series and wavelet in Fig. 9 show that individual inception events are in general easily discerned. Additionally, results presented later in Fig. 14 highlights the difference between the background acoustic pressure fluctuations of the filtered signal and small incipient events. Nevertheless, it cannot be asserted that all incipient events are measured as some very small nuclei growth may fall below this value, and for cavitation numbers well below inception, a single event will still be measured multiple times if it persists longer than 10 ms. However, high-speed photography when coupled with the acoustic data suggests that nuclei that experience sufficient growth so as to become visible are all captured via the counting method used.

The acoustic event rate across the investigated range of τ and σ are presented in Fig. 12. As the overall SPL is dominated by the loud acoustic events, the event rate follows a similar trend to that observed in Fig. 11(a). However, from Fig. 12, it is evident that, although cavitation is quieter in an integral sense, the trend in the event rate remained consistent for $\sigma \leq 2$ for all but the smallest gap. From the observations in the high-speed imaging, this may be attributable to an increase in traveling bubble cavitation within the gap.

From the bottom plot in Fig. 12, it can be observed that the increase in the event rate approximately follows a log-linear trend with a decrease in σ . This can be associated with a larger proportion of the nuclei contained within the natural population—which follows a power law—being activated with the reduction in pressure. The variation in the event rate is approximately three orders of magnitude across the range of tested σ . In addition, it is apparent that the flow behavior changes for $\tau \leq 0.2$, as these curves show substantial deviation from the observed trend. This is attributed to a dramatic

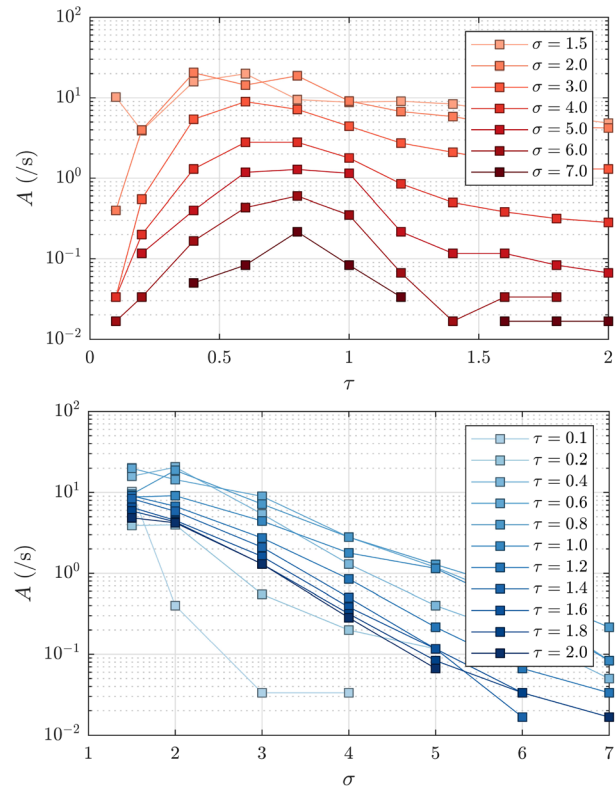


FIG. 12. Acoustic cavitation event rate for unseeded flow for a range of σ and τ at $\alpha = 6^\circ$ and $Re = 3 \times 10^6$. The same data are presented in both plots with a different variable on the x-axis.

reduction of flow rate through the gap leading to higher pressures in the tip leakage vortex.

A graphical summary of the features observed for the natural nuclei population is presented in Fig. 13. Two contours have been superimposed on the graph to delineate characteristic regions of the parameter map. In the region far left of the map, the very loud collapse phenomenon of Fig. 10 dominates, and cavitation is well developed. In the center region, incipient cavities grow to fill the leakage vortex, but not with such regularity or violence as to produce loud pressure peaks. The first contour marked with solid line indicates where the very loud collapse phenomenon produces a maximum absolute pressure value of above 2400 kPa anywhere in the 1 kHz high-pass filtered signal. In the region right of second dashed contour line, cavitation is a rare event and grows only slightly in size. The dashed line separates when the activation rate fell below 0.1 events per second. The activation rate of one event every 10 s was chosen based on the overall length of the hydrophone data recorded (60 s) in order to balance pragmatic requirements that sample duration could not be overly long, while also ensuring the developed contour was not inappropriately represented by the observation of an improbable arrival rate during the sample. During these measurements, high-speed footage was recorded, but its duration was much shorter than the acoustic data. This meant that for most recordings no events were captured in the high-speed footage; yet, the acoustic event rate was often not zero.

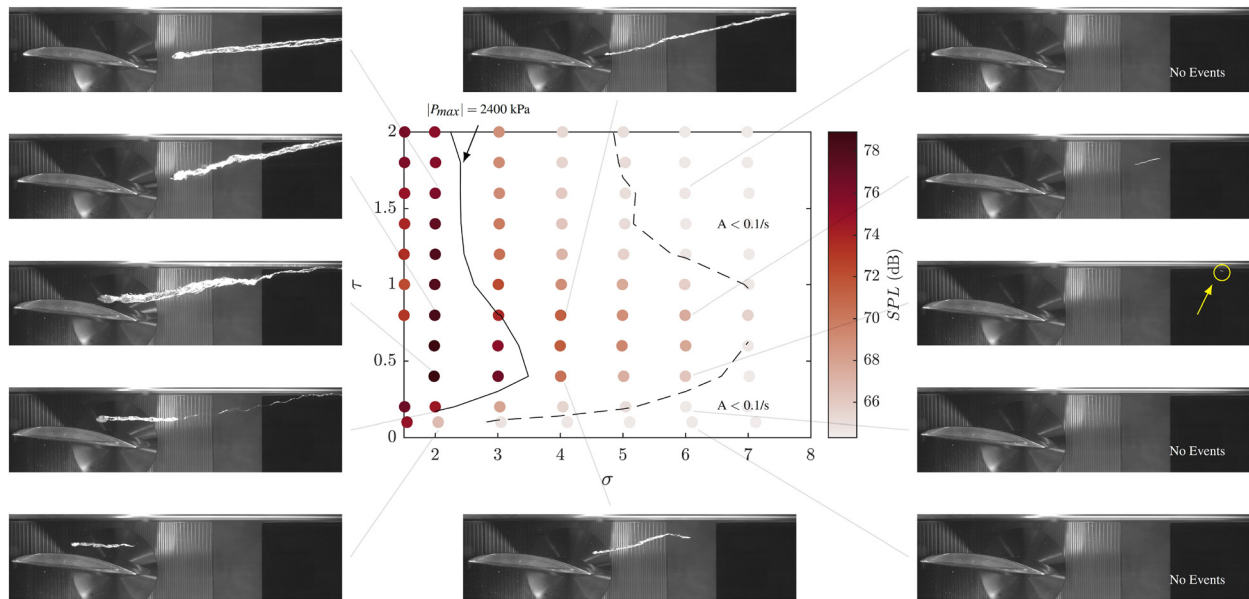


FIG. 13. Summary of cavitation topology and inception in tip leakage for the natural nuclei population. The colored points indicate the overall sound pressure level. The solid contour indicates a maximum acoustic pressure of 2400 Pa. The dashed contour line indicates an activation rate of 0.1/s.

Incipient cavitation events in a nuclei abundant flow

To investigate the effect of higher nuclei concentrations on the TLF cavitation, measurements were repeated with the flow seeded with the abundant population, as presented in Fig. 11(b). This population is characterized by a nuclei concentration of $N_b \approx 10 \text{ ml}^{-1}$. For dense seeding, the TLV is continuously fed with microbubbles that accumulate in the vortex core. It can be seen that the variation in SPL for a fixed τ was lower for the seeded flow ($\approx 5 \text{ dB}$) than for the natural nuclei population ($\approx 15 \text{ dB}$). In addition, a gradual shift in the location of the peak in SPL toward the lower τ values is seen with a decrease in σ .

A change in the trend of SPL with variation in τ can be observed at $\tau \approx 0.6$. Greater SPL is seen for the cases with a low σ and small τ . This is attributed to increased fragmentation and oscillations of the main cavity volume due to the perturbations induced by proximity of the tip to the tunnel ceiling and associated wall boundary layer. Additionally, isolated traveling bubble cavities within the gap contribute to the SPL. For $\sigma \geq 4$, cavitation in the gap does not form for small τ so that greater SPL were observed for higher τ values. The comparison of SPL between the natural and abundant nuclei population highlights the complexity that the variation in the nuclei content adds to the flow. For high σ , an increase in the freestream nuclei content is accompanied by a rise in SPL. In contrast, for low σ , the SPL is greater for the flow with natural nuclei population. These differences can be explained by analyzing the respective time series of the acoustic data.

A comparison of cavitation topology and acoustic signature of the TLF for the natural nuclei and seeded flow is presented in Fig. 14. Time series segments that have been 1 kHz high-pass filtered are shown alongside representative images of the cavitation topology extracted from high-speed imaging for $\sigma = \{2, 4, 6\}$ at $\tau = 0.8$. In addition, histograms of the probability of observing instantaneous pressure values within the time series are plotted in Fig. 14(c). At $\sigma = 2$,

the extremely loud collapse events (from an incipient cavity merging with the downstream cavity) occur often in the natural nuclei flow, while the seeded flow is characterized by a consistent but relatively inactive leakage vortex cavity. The scale and regularity of instantaneous pressures observed in these data are expressed as a probability density function of the absolute value of the (high-pass filtered) pressure amplitude. These have been plotted with a logarithmic probability scale for the colored data to ensure that rare loud events are discernible. A linear probability scale for the same data has been superimposed with a black line so that mean pressures can be easily interpreted. These plots show that on average, the natural nuclei and seeded flows have similar instantaneous pressure values for $\sigma = 2$, but it is the acoustic magnitude of the merge/collapse events that increases the overall SPL.

As σ increases, the loud collapse events become less frequent and the SPL of the seeded flow surpasses that of the flow with the natural nuclei. This can be attributed to an elevated baseline SPL associated with the presence of a continuous TLV cavity in seeded flow, in comparison to the lower baseline SPL during the periods without cavitation in the natural nuclei flow. Additionally, a slight increase in the baseline SPL with a decrease in σ is noticeable for the seeded flow. This can be attributed to a lesser opportunity for growth of the activated nuclei before joining the main cavity, due to a shift of the main cavity leading edge closer to the hydrofoil with a decrease in σ .

In summary, for the natural nuclei population, noise levels are controlled by the activation rate and the much louder vortex cavity merging events. Both the intensity and rate of these increase with decreasing cavitation number and reach a peak for a particular tip gap. In flows with abundant nuclei, noise levels are controlled by continuous sources, presumably due to local dynamic behavior of the globally stable vortex cavity. There is a clear crossover between the combined effects of σ , nuclei concentration, and size, which is modulated by the

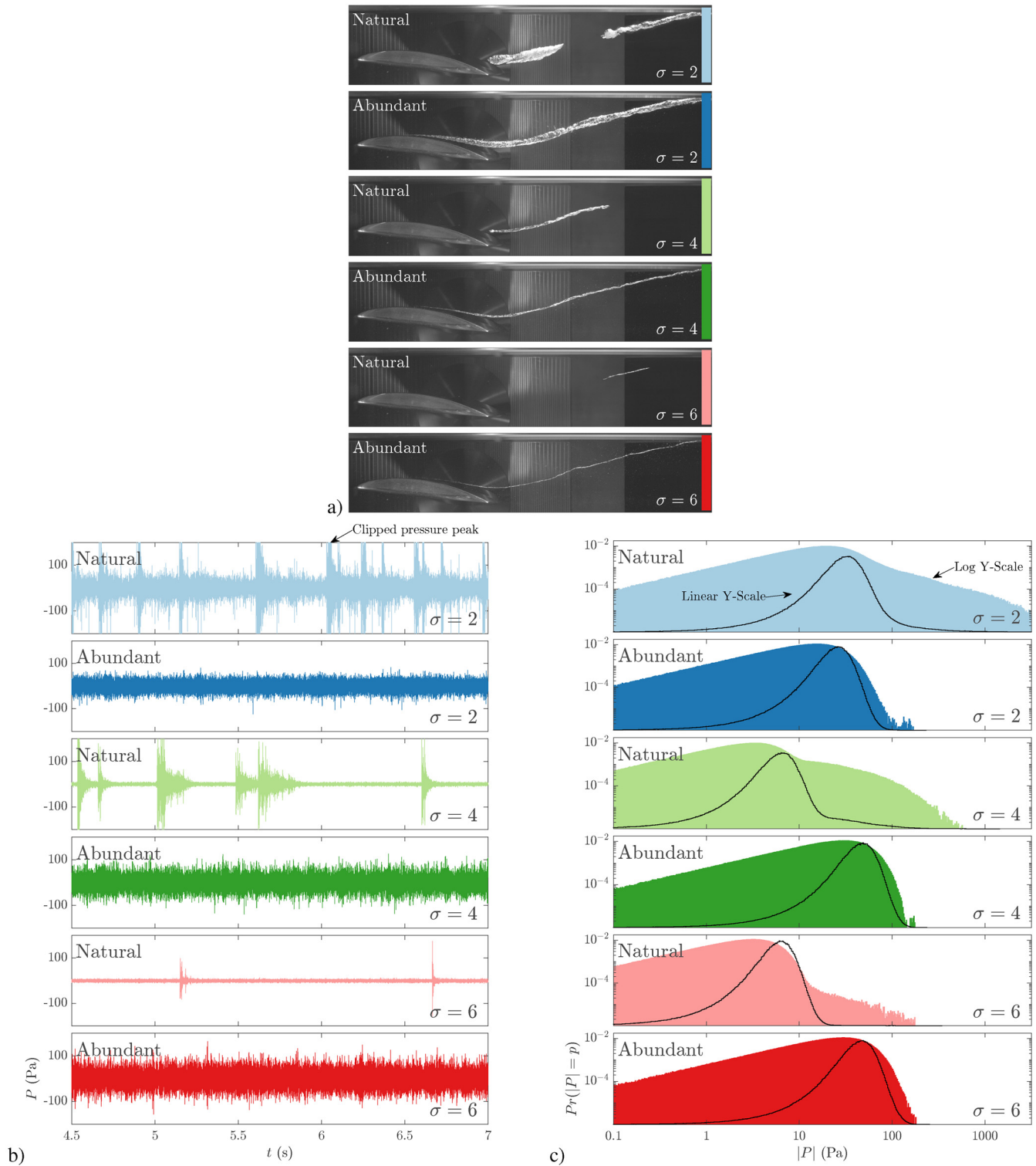


FIG. 14. Comparison of cavitation topology and acoustic signature for both the natural and abundant nuclei populations at $\sigma = \{2, 4, 6\}$ is presented. (a) Sample images of the cavitation topology for each condition, (b) time series of acoustic pressure high-pass filtered with a 1 kHz cutoff frequency, and (c) probability density function for the instantaneous pressure in the high-pass filtered acoustic data. The data are plotted on both a linear and logarithmic scale.

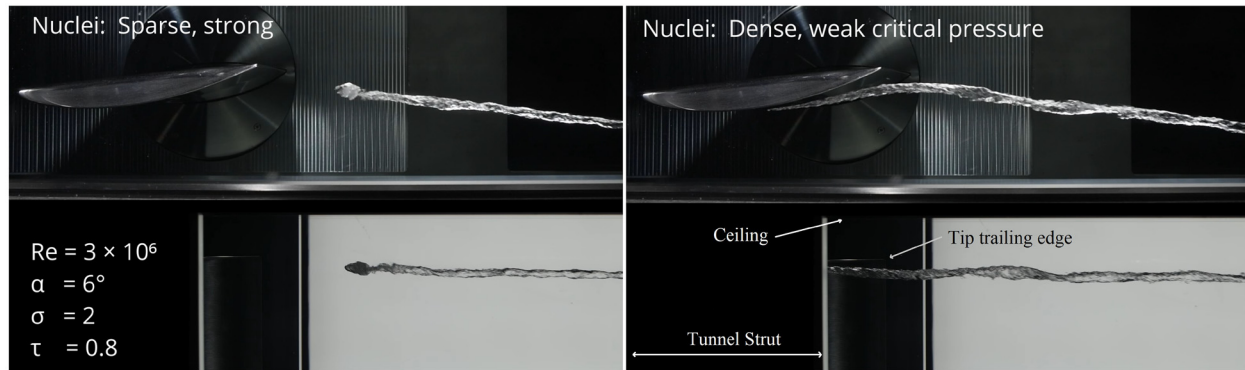


FIG. 15. The effect of nuclei for otherwise identical conditions is presented through a composite video recorded using two DSLR cameras. Multimedia view: <https://doi.org/10.1063/5.0132034.2>

gap height. The importance of nuclei when investigating these flows should be emphasized and is perhaps best achieved through a pair of simultaneous recordings using a DSLR camera. The sound heard by the experimenter outside the tunnel was captured with the in-built camera microphone. One was positioned above the tunnel, while the other viewed the tip gap flow from the side. During the recording, the nuclei seeding system is turned on and the effect of additional free-stream nuclei is apparent in Fig. 15 (Multimedia view).

Further investigation is needed to explore how this change transitions for intermediate nuclei populations. These results agree with the findings of Dreyer *et al.*,²¹ that there is an intermediate gap height ratio with poor cavitation performance that varies with incidence. Additionally, in terms of acoustic performance, this value also changes with the availability of freestream nuclei.

CONCLUSION

The effect of nucleation on a tip leakage flow was investigated in a variable pressure water tunnel using a stationary hydrofoil analogy. Experiments were performed utilizing two distinct free-stream nuclei conditions: a sparse population of nuclei with strong critical pressures and an abundant population of nuclei with weak critical pressures.

The topology of the developed cavitation was characterized for a wide range of τ and α values. For large τ and small α , cavitation was observed in the tip leakage vortex and resembled tip vortex cavitation characteristic of an unbounded flow around a three-dimensional hydrofoil. With an increase in α , cavitation topology became more complex, with secondary vortical structures originating from the tip trailing edge and jetting shear layer on the suction side of the hydrofoil interacting with the leakage vortex. For high α and small τ , traveling bubble and attached cavitation was observed within the gap. Generally, the cavitation in natural nuclei flow was observed to have an intermittent character, becoming more continuous with the introduction of seeding.

Based on the observations of the cavity topology, an incidence of $\alpha = 6^\circ$ was chosen for further characterization using acoustic measurements. From these, a critical gap clearance with the highest incipient cavitation number in the natural nuclei flow was found for $\tau = 0.8$. For the seeded flow, cavitation was persistent at the highest cavitation numbers achievable in the experimental facility, and inception was not fully resolved.

Acoustic measurements reveal a higher baseline acoustic signature for the seeded flow, stemming from the presence of a continuous cavity. The intermittent character of cavitation for the natural nuclei flow gives a lower baseline noise. However, the collapse associated with merging between successive cavitation events was observed as a flow feature with the highest instantaneous peaks in acoustic pressure.

The influence of nucleation was examined for the two extremes of nuclei populations in which turbomachinery and ducted propulsors typically operate. Such an approach highlights the significant effects the nuclei population may have on the occurrence of cavitation in tip leakage flows. Future efforts will concentrate on characterization of cavitation inception and dynamics across a range of intermediate poly- and monodisperse nuclei populations.

SUPPLEMENTARY MATERIAL

See the [supplementary material](#) for a 3D model of the hydrofoil geometry used in the experiments, outlined in Fig. 3 and illustrated within Fig. 4.

ACKNOWLEDGMENTS

This project was supported by the Australian Defence Science and Technology Group (DSTG), and the US Office of Naval Research and ONR Global through NICOP S&T Grant No. N62909-19-1-2062, and the 2019 U.S. Multidisciplinary University Research Initiative (MURI)—Program managers Ki-Han Kim, Sung-Eun Kim, and Julie Young. The authors are grateful for the technical assistance provided by Mr. Steven Kent and Mr. Robert Wrigley when conducting these experiments.

AUTHOR DECLARATIONS

Conflict of Interest

The authors have no conflicts to disclose.

Author Contributions

Patrick Russell: Conceptualization (equal); Data curation (equal); Formal analysis (equal); Methodology (equal); Validation (equal); Visualization (equal); Writing – original draft (equal). **Luka Barbaca:** Data curation (equal); Formal analysis (equal); Methodology (equal);

Validation (supporting); Visualization (supporting); Writing – original draft (equal); Writing – review & editing (equal). **James Venning:** Data curation (equal); Formal analysis (equal); Methodology (equal); Validation (equal); Visualization (equal); Writing – original draft (supporting); Writing – review & editing (supporting). **Bryce Pearce:** Conceptualization (equal); Data curation (equal); Formal analysis (equal); Funding acquisition (lead); Project administration (equal); Resources (equal); Writing – original draft (equal); Writing – review & editing (equal). **Paul Brandner:** Conceptualization (lead); Data curation (equal); Formal analysis (equal); Funding acquisition (lead); Methodology (equal); Project administration (equal); Writing – original draft (equal); Writing – review & editing (equal).

DATA AVAILABILITY

Raw data were generated at the Australian Maritime College Cavitation Research Laboratory large scale facility. The data that support the findings of this study are available within the article.

REFERENCES

- ¹H. Cheng, B. Ji, X. Long, W. Huai, and M. Farhat, “A review of cavitation in tip-leakage flow and its control,” *J. Hydrodyn.* **33**, 226–242 (2021).
- ²Y. Zhou, G. Pavesi, J. Yuan, and Y. Fu, “A review on hydrodynamic performance and design of pump-jet: Advances, challenges and prospects,” *J. Mar. Sci. Eng.* **10**, 1514 (2022).
- ³G. F. Oweis and S. L. Ceccio, “Instantaneous and time-averaged flow fields of multiple vortices in the tip region of a ducted propulsor,” *Exp. Fluids* **38**, 615–636 (2005).
- ⁴H. Wu, D. Tan, R. L. Miorini, and J. Katz, “Three-dimensional flow structures and associated turbulence in the tip region of a waterjet pump rotor blade,” *Exp. Fluids* **51**, 1721–1737 (2011).
- ⁵N. A. Chang, J. Choi, R. Yakushiji, and S. L. Ceccio, “Cavitation inception during the interaction of a pair of counter-rotating vortices,” *Phys. Fluids* **24**, 014107 (2012).
- ⁶S. Gopalan, J. Katz, and O. Knio, “The flow structure in the near field of jets and its effect on cavitation inception,” *J. Fluid Mech.* **398**, 1–43 (1999).
- ⁷B. Ran and J. Katz, “Pressure fluctuations and their effect on cavitation inception within water jets,” *J. Fluid Mech.* **262**, 223–263 (1994).
- ⁸T. J. O’Hern, “An experimental investigation of turbulent shear flow cavitation,” *J. Fluid Mech.* **215**, 365–391 (1990).
- ⁹E. Allan, L. Barbaca, P. S. Russell, J. A. Venning, B. W. Pearce, and P. A. Brandner, “The influence of nucleation on cavitation inception in turbulent shear layers,” in 34th Symposium on Naval Hydrodynamics, 2022.
- ¹⁰K. Agarwal, O. Ram, Y. Lu, and J. Katz, “On the unsteady pressure field, nuclei dynamics and cavitation inception in a turbulent shear layer,” in 34th Symposium on Naval Hydrodynamics, 2022.
- ¹¹E. Allan, L. Barbaca, J. A. Venning, P. S. Russell, B. W. Pearce, and P. A. Brandner, “Nucleation and cavitation inception in high Reynolds number shear layers,” *Phys. Fluids* **35**, 013317 (2022).
- ¹²S. Green and A. Acosta, “Unsteady flow in trailing vortices,” *J. Fluid Mech.* **227**, 107–134 (1991).
- ¹³O. Boulon, J. Franc, and J. Michel, “Tip vortex cavitation on an oscillating hydrofoil,” *J. Fluids Eng.* **119**, 752–758 (1997).
- ¹⁴D. You, M. Wang, P. Moin, and R. Mittal, “Effects of tip-gap size on the tip-leakage flow in a turbomachinery cascade,” *Phys. Fluids* **18**, 105102 (2006).
- ¹⁵P. S. Russell, L. Barbaca, E. S. C. Russell, B. W. Pearce, and P. A. Brandner, “Cavitation in tip-leakage flows,” in 33rd Symposium on Naval Hydrodynamics, 2020.
- ¹⁶R. Laborde, P. Chantrel, and M. Mory, “Tip clearance and tip vortex cavitation in an axial flow pump,” *J. Fluids Eng.* **119**, 680–685 (1997).
- ¹⁷M. Dreyer, “Mind the gap: Tip leakage vortex dynamics and cavitation in axial turbines,” Ph.D. thesis [Swiss Federal Institute of Technology in Lausanne (EPFL), 2015].
- ¹⁸O. Boulon, M. Callenaere, J. Franc, and J. Michel, “An experimental insight into the effect of confinement on tip vortex cavitation of an elliptical hydrofoil,” *J. Fluid Mech.* **390**, 1–23 (1999).
- ¹⁹S. Gopalan, J. Katz, and H. L. Liu, “Effect of gap size on tip leakage cavitation inception, associated noise and flow structure,” *J. Fluids Eng.* **124**, 994–1004 (2002).
- ²⁰S. Higashi, Y. Yoshida, and Y. Tsujimoto, “Tip leakage vortex cavitation from the tip clearance of a single hydrofoil,” *JSME Int. J. Ser., B* **45**, 662–671 (2002).
- ²¹M. Dreyer, J. Decaix, C. Mönch-Alligné, and M. Farhat, “Mind the gap: A new insight into the tip leakage vortex using stereo-PIV,” *Exp. Fluids* **55**, 1849 (2014).
- ²²D. You, M. Wang, P. Moin, and R. Mittal, “Vortex dynamics and low-pressure fluctuations in the tip-clearance flow,” *J. Fluids Eng.* **129**, 1002–1014 (2007).
- ²³D. Zhang, W. Shi, B. van Esch, L. Shi, and M. Dubuisson, “Numerical and experimental investigation of tip leakage vortex trajectory and dynamics in an axial flow pump,” *Comput. Fluids* **112**, 61–71 (2015).
- ²⁴Q. Guo, L. Zhou, and Z. Wang, “Numerical evaluation of the clearance geometries effect on the flow field and performance of a hydrofoil,” *Renewable Energy* **99**, 390–397 (2016).
- ²⁵Z. Qian, Z. Wang, C. Geng, and X. Luo, “Vortex and cavity dynamics for the tip-leakage cavitation over a hydrofoil,” *Phys. Fluids* **34**, 093303 (2022).
- ²⁶P. A. Brandner, J. A. Venning, and B. W. Pearce, “Nucleation effects on cavitation about a sphere,” *J. Fluid Mech.* **946**, A1 (2022).
- ²⁷J. A. Venning, B. W. Pearce, and P. A. Brandner, “Nucleation effects on cloud cavitation about a hydrofoil,” *J. Fluid Mech.* **947**, A1 (2022).
- ²⁸M. T. Khoo, J. A. Venning, B. W. Pearce, and P. A. Brandner, “Nucleation and cavitation number effects on tip vortex cavitation dynamics and noise,” *Exp. Fluids* **62**, 216 (2021).
- ²⁹P. S. Russell, L. Barbaca, J. A. Venning, B. W. Pearce, and P. A. Brandner, “Nucleation effects on tip-gap cavitation,” in 22nd Australasian Fluid Mechanics Conference (AFMC2020), 2020.
- ³⁰R. E. A. Arndt and B. H. Maines, “Viscous effects in tip vortex cavitation and nucleation,” in 20th Symposium on Naval Hydrodynamics, 1994.
- ³¹L. Briancon-Marjollet and L. Merle, “Inception, development and noise of a tip vortex cavitation,” in 21st Symposium on Naval Hydrodynamics, 1996.
- ³²X. Peng, L. Xu, and Y. Cao, “The study of tip vortex flow and cavitation inception on an elliptical hydrofoil,” in 5th International Symposium on Marine Propulsion, 2017.
- ³³M. Drela, “XFOIL: An analysis and design system for low Reynolds number airfoils,” in *Low Reynolds Number Aerodynamics* (Springer, 1989), pp. 1–12.
- ³⁴P. A. Brandner, Y. Lecoffre, and G. J. Walker, “Development of an Australian national facility for cavitation research,” in Sixth International Symposium on Cavitation (CAV 2006), 2006.
- ³⁵P. A. Brandner, Y. Lecoffre, and G. J. Walker, “Design considerations in the development of a modern cavitation tunnel,” in 16th Australasian Fluid Mechanics Conference (16AFMC), 2007.
- ³⁶A. Belle, P. A. Brandner, B. W. Pearce, K. L. de Graaf, and D. B. Clarke, “Artificial thickening and thinning of cavitation tunnel boundary layers,” *Exp. Therm. Fluid Sci.* **78**, 75–89 (2016).
- ³⁷P. Russell, B. Pearce, and P. Brandner, “A method for generating lifting surface profiles from simplified parametric equations,” in Proceedings of the 23rd Australasian Fluid Mechanics Conference, 2022.
- ³⁸C. Doolan, P. Brandner, D. Butler, B. Pearce, D. Moreau, and L. Brooks, “Hydroacoustic characterization of the AMC cavitation tunnel,” in Acoustic, Victor Harbour, Australia, 2013.
- ³⁹M. T. Khoo, J. A. Venning, B. W. Pearce, K. Takahashi, T. Mori, and P. A. Brandner, “Natural nuclei population dynamics in cavitation tunnels,” *Exp. Fluids* **61**, 34 (2020).
- ⁴⁰L. Barbaca, P. S. Russell, B. W. Pearce, and P. A. Brandner, “Characterization of microbubble generation in a confined turbulent jet,” in Proceedings of the 22nd Australasian Fluid Mechanics Conference, 2020.
- ⁴¹P. S. Russell, L. Barbaca, J. A. Venning, B. W. Pearce, and P. A. Brandner, “Measurement of nuclei seeding in hydrodynamic test facilities,” *Exp. Fluids* **61**, 79 (2020).